Soft Matter

PAPER

View Article Online
View Journal | View Issue

Cite this: *Soft Matter*, 2024, **20**, 4988

Highly porous hydrogels for efficient solar water evaporation†

Akash Ranjan Pati,[a] Young-Su Ko,[a] Changwoo Bae,[a] Inhee Choi,[b] Yun Jung Heo*[ac] and Choongyeop Lee*[a]

Solar energy is a plentiful renewable resource on Earth, with versatile applications in both domestic and industrial settings, particularly in solar steam generation (SSG). However, current SSG processes encounter challenges such as low efficiency and the requirement for extremely high concentrations of solar irradiation. Interfacial evaporation technology has emerged as a solution to these issues, offering improved solar performance compared to conventional SSG processes. Nonetheless, its implementation introduces additional complexities and costs to system construction. In this study, we present the development of hydrophilic, three-dimensional network-structured hydrogels with high porosity and swelling ratio using a facile fabrication technique. We systematically varied the mixing ratios of four key ingredients (polyethylene glycol diacrylate, PEGDA; polyethylene glycol methyl-ether acrylate, PEGMA; phosphate-buffered saline, PBS; and 2-hydroxy-2-methylpropiophenone, PI) to control the mean pore size and swelling ratio of the hydrogel. Additionally, plasmonic gold nanoparticles were incorporated into the hydrogel using a novel methodology to enhance solar light absorption and subsequent evaporation efficiency. The resulting material exhibited a remarkable solar efficiency of 77% and an evaporation rate of 1.6 kg m^{-2} h^{-1} under standard solar illumination (one sun), comparable to those of state-of-the-art SSG devices. This high efficiency can be attributed to the synergistic effects of the hydrogel's unique composition and nanoparticle concentration. These findings offer a promising avenue for the development of highly efficient solar-powered evaporation applications.

Received 3rd April 2024,
Accepted 3rd June 2024

DOI: 10.1039/d4sm00388h

rsc.li/soft-matter-journal

Introduction

The onset of the industrial revolution and the rise in domestic demands have elevated water scarcity to one of the paramount challenges of modern times.[1,2] Despite oceans covering the majority of the Earth's surface, their vast water resources remain unfit for human consumption. This dilemma has prompted numerous scientists and researchers to explore a variety of solar and renewable technologies with the aim of making ocean water potable or devising efficient and cost-effective methods for water production.[1] Solar-driven steam generation (SSG) has garnered significant attention in recent years due to its versatility, encompassing applications such as electricity generation, salt harvesting, steam production, and desalination.[3]

Conventional SSG methods typically necessitate a very high optical concentration (C_{opt}) to generate steam, either by directly utilizing the bulk liquid or through an intermediate carrier fluid. However, this approach adds complexity and cost to the system.[4–6] In contrast, the recently developed interfacial solar evaporation technology represents a promising advancement in SSG. This method offers superior steam production efficiency by localizing heat at the interface, resulting in high solar-to-heat conversion efficiency.[3] This can be achieved by illuminating a porous solar-absorbing material positioned on the surface of water or seawater, rather than directly irradiating the bulk water. This approach enhances both efficiency and evaporation rates, making interfacial solar evaporation an attractive alternative for steam generation.

For efficient steam generation, interface materials must possess specific properties conducive to efficient evaporation, such as a high specific area for evaporation, a hydrophilic photothermal surface, and an abundance of pores for fluid transport from the bulk.[7] Various materials, such as carbon-based materials,[8,9] plasmonic nanoparticles,[10,11] and bio-inspired nanostructures,[12] have been explored as interface materials to enhance the photothermal efficiency in comparison to those of conventional SSG processes.[11,13] Leveraging the distinctive optical

[a] *Department of Mechanical Engineering (Integrated Engineering Program), Kyung Hee University, Yongin-si 17104, Republic of Korea. E-mail: yunjheo@khu.ac.kr, cylee@khu.ac.kr*
[b] *Department of Life Sciences, University of Seoul, Seoul 02504, Republic of Korea*
[c] *Integrated Education Institute for Frontier Science & Technology (BK21 Four), Kyung Hee University, Yongin-si 17104, Republic of Korea*

† Electronic supplementary information (ESI) available. See DOI: https://doi.org/10.1039/d4sm00388h

properties of nanoparticles allows for the swift and effective conversion of light energy into thermal energy, thereby enhancing evaporation rates significantly.[14] Carbon nanotubes, graphene, metal nanoparticles, and hybrid nanomaterials are among the extensively researched nanoparticles due to their exceptional photothermal properties and adaptable surface chemistry. These nanoparticles not only absorb a broad range of light wavelengths but also exhibit efficient thermal conversion and robust photothermal stability. Nonetheless, it is important to acknowledge that nanoparticles present challenges related to cost and a tendency to fuse, which currently restrict their practical applicability.[15,16] In contrast, hydrogels have emerged as preferred materials for solar steam generation (SSG) processes due to their exceptional properties, including a high swelling ratio, excellent light transmittance, thermal stability, porous structures, and flexibility, and cost-effectiveness. By harnessing these attributes, hydrogels provide a sustainable and efficient means to enhance water evaporation and produce clean & renewable steam.

Notably, various studies have successfully improved evaporation rates using different hydrogels and layered materials. Sun *et al.*[17] developed a crosslinked acrylic acid and acrylamide self-healing hydrogel with enhanced light utilization for solar water evaporation, achieving a 1.58 kg m^{-2} h^{-1} evaporation rate and the ability to self-heal and stretch significantly, which is promising for durable outdoor use. Similarly, the Sun group[18] developed a copper sulfide-macroporous polyacrylamide hydrogel (CuS-m-PAM) that enhances solar steam generation, achieving up to 92% solar photothermal conversion efficiency. Developed *via in situ* synthesis, this material effectively localizes heat and maintains high performance and stability. Zhu *et al.*[19] prepared chitosan/polyvinyl alcohol and carbon nanoparticle double layer hydrogels, achieving an excellent evaporation rate of 2.28 kg m^{-2} h^{-1}. Zhou *et al.*[20] demonstrated a solar evaporator utilizing a hydrophilic polymer and a reduced graphene oxide hydrogel, capable of producing vapor at a high rate of 2.5 kg m^{-2} h^{-1} under one sun irradiation. Because of the reduced vaporization enthalpy within the CNTs/starch hybrid biohydrogel, Xu *et al.*[21] developed a composite Janus-carbon nanotube/polyvinyl alcohol hydrogel and achieved a high evaporation rate of 2.77 kg m^{-2} h^{-1}, with an efficiency of approximately 88% under 1.0 sun irradiation. A recent study[22] introduced a hydrogel-based evaporator using a hydrophilic, porous light-absorber, $C_2N_xO_{1-x}$, for solar-powered water purification, achieving an evaporation rate of 2.9 kg m^{-2} h^{-1}. In a separate work, Sun *et al.*[23] and Guo *et al.*[24] introduced nanoparticles into the hydrogels to enhance the solar evaporation rates. Moreover, polymeric coatings such as polypyrrole[11] and polydopamine[25] have been employed as photo materials in SSG processes. Chen *et al.*[26] introduced a novel polymer foam, poly(1,3,5-hexahydro-1,3,5-triazine) (PHT), for solar evaporation experiments, achieving impressive evaporation rates (1.2 kg m^{-2} h^{-1}) and efficiency (80%). The Lin group[27] demonstrated the utility of melamine foams as integrative solar absorbers (ISAs), yielding an evaporation rate of 1.27 kg m^{-2} h^{-1} under 1-sun illumination. Although the evaporation rates and efficiencies demonstrated by these hydrogels and foam materials are impressive, their preparation processes are intricate and pose challenges in terms of reproducibility. The complexity of synthesizing these materials may hinder consistent production on a large scale, potentially limiting their widespread adoption in practical applications.

In general, hydrogels exhibit low porosity, necessitating additional methods[28] such as salt leaching[29] and pore foaming[30] to render them suitable for the SSG process, thereby increasing the complexity of fabrication. Moreover, commonly employed hydrogel materials for SSG in the literature often feature double layered or multiple layer structures, constraining practical scalability.[25] To date, few reports have explored single-layer material hydrogels exclusively for the SSG process. Thus, this study introduces a scalable, cost-effective, and semi-transparent highly porous single-layer hydrogel structure using polyethylene glycol diacrylate (PEGDA), polyethylene glycol methyl-ether acrylate (PEGMA), phosphate-buffered saline (PBS), and 2-hydroxy-2-methylpropiophenone (photoinitiator, PI). We optimize the hydrogel mixing ratio to achieve a porosity exceeding 90% and an excellent swelling ratio. As the hydrogel is denser than water, we utilize a mesh to suspend it at the air–water interface, while reinforcing the hydrogel's mechanical strength. Furthermore, the incorporation of Au ions into the hydrogel solution enhances its photothermal evaporation capabilities, stemming from a photoreduction reaction involving Au ions, the hydrogel, and UV radiation, leading to the formation of AuNPs. By optimizing the Au ion concentration in the hydrogel, significant improvements in evaporation rates are achieved under both one and two sun illumination conditions. The key advancement of this research is the implementation of a semi-transparent single-layer structure, which not only acts as a solar absorber and facilitates water delivery to the interface but also incorporates Au ions to enhance the evaporation rate further.

Results and discussion

In the current investigation, experiments are conducted using an interfacial solar steam generation setup illustrated in Fig. 1a, under 1 and 2 sun illumination (C_{opt}) at room temperature and humidity of 22 ± 3 °C and 23 ± 2%, respectively. Prior to the experiment, the setup was placed in a high precision weighing balance (±0.001 g) to record the mass loss throughout the entire evaporation process, with the evaporation rates measured every minute over a duration of 3 hours. Each evaporation test was conducted three times to confirm the reliability and repeatability of the data. The setup primarily comprises a PEGDA hydrogel crosslinked with PEGMA, combined with PBS and a photo initiator on the mesh affixed to an acrylic sheet (~1 mm thick), as illustrated in Fig. 1a (see also Fig. S1a and b, ESI†, and the materials and methods section for details of the preparation). An as-received copper mesh (#50) serves as a mechanical support for the hydrogel and is utilized to suspend it at the air–water interface to facilitate efficient evaporation. Furthermore, the mesh does not hinder water uptake from the reservoir. The effect of the mesh on the evaporation process is elucidated through control experiments, as demonstrated in Fig. S2 and the Supplementary Notes (ESI†). The prepared sample is denoted as the PEGDA/PEGMA hydrogel (Fig. S1b, ESI†).

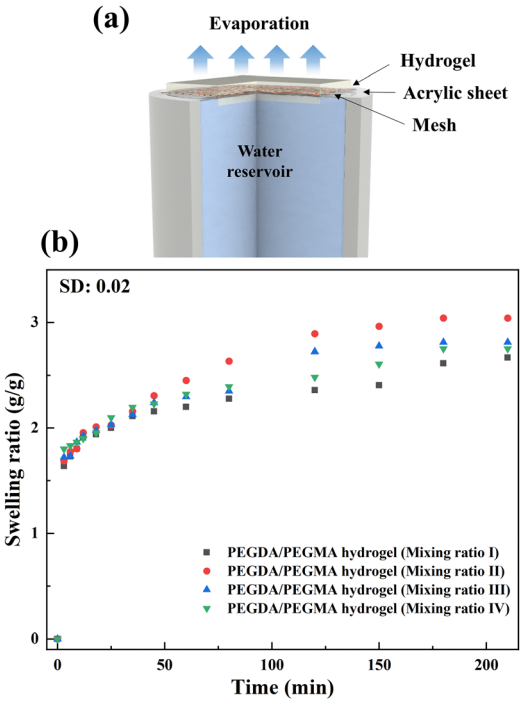

Fig. 1 (a) Schematic illustration of the solar steam generation setup. (b) swelling ratio over time of hydrogel samples prepared with different mixing ratios.

Optimization of the mixing ratio

The structural integrity of the hydrogel is enhanced by the PEGDA monomer, which establishes a 3D network of interconnected polymer chains, while both PEGDA and PEGMA contribute to the hydrogel's hydrophilicity. The combination of these polymers proves optimal for the present solar evaporation process, which necessitates properties such as continuous water replenishment, a higher number of pores and improved wettability. In the current experiments, PBS is included alongside PEGDA, PEGMA and the photo initiator (PI). We use PBS instead of water in the preparation of the composite hydrogel to prevent excessive swelling, which could lead to surface flooding, undesirable for efficient evaporation.[31,32]

To optimize various combinations of mixing ratios, swelling ratios are measured and shown in Fig. 1b (see the materials and methods section for the equation). It is found that mixing ratio II exhibits the highest swelling ratio, attributed to the inclusion of the PEGMA monomer (50% v/v) in the PEGDA hydrogel, leading to an increase in the number of pores in the composite hydrogel network.[33–35] For further verification, the porosity of the hydrogels is determined by using the equations provided by Zu *et al.*[36] This analysis confirms that the PEGDA/PEGMA hydrogel (mixing ratio II) exhibits the highest porosity of 90 ± 0.8%. Furthermore, the presence of an adequate amount of the photo initiator (the highest among all mixing ratio) under UV light creates free radicals for crosslinking the polymers, establishing a 3D networking structure that facilitates water channel formation[37] (Table 1). Comparison of mixing ratio II and III also reveals that even with the same monomer concentrations, a smaller amount of photo initiator in ratio III results in a lower swelling ratio compared to that for ratio II (Fig. 1b). Nevertheless, the swelling ratio is highly influenced by the concentration of PEGMA in PBS.[38] As the concentration of PEGMA decreases, the swelling ratio increases, which is evident from Table 1. Furthermore, to assess the water absorption capacity and identify the optimal hydrogel combination, control evaporation experiments are conducted for all mixing ratios.

Table 1 Tested mixing ratios of the hydrogel (per 10 mL)

Mixing ratio	PEGMA (mL)	PEGDA (mL)	PBS (mL)	Photo initiator (mL)
I	2.5	2.5	5	0.25
II	1.5	1.5	7	0.60
III	1.5	1.5	7	0.50
IV	2.25	0.75	7	0.15

Fig. 2a demonstrates calculated evaporation rates of 1.18, 1.36, 1.32 and 1.31 kg m^{-2} h^{-1} for mixing ratios I, II, III and IV, respectively. These rates are determined from the slope of the mass loss *vs.* time curve. Notably, the maximum mass loss occurs in the case of the PEGDA/PEGMA hydrogel (mixing ratio II). Based on the above analysis, after considering both the swelling ratio and evaporation rates, it is evident that the mixing ratio II represents the optimal hydrogel combination. The balance of sufficient water content and high porosity facilitates efficient water transport from the bulk water to the liquid–air interface.[39] Therefore, mixing ratio II is consistently used in all subsequent evaporation experiments.

Determination of optimum hydrogel thickness

Fig. 2b depicts the rate of mass loss of the PEGDA/PEGMA hydrogel at various hydrogel thickness (t = 0.73, 2, 2.8 and 3.8 mm), with the mass loss of bulk water also included for comparison. It is evident that the rate of mass loss increases with thickness up to 2.8 mm, beyond which it begins to decline. This trend suggests that up to 2.8 mm thickness, water molecules may find it easier to locate the evaporation path, such that water molecules move and evaporate more quickly within the hydrogel structure. This phenomenon aligns with the photo-molecular theory previously reported for such processes.[40,41] According to this theory, when solar incident light impacts the hydrogel surface, it penetrates and disrupts water clusters within the 3D network,[33] initiating evaporation. Upon measuring the temperature at the interface, we observed a slight increase, attributed to the disintegration of water clusters as they collided with air molecules, resulting in heat absorption (Fig. 2c). Once a molecular cluster detaches from the surface, it will encounter other vapor and air molecules, altering its trajectory and/or causing the molecules within the cluster to disperse or recombine with water or hydrogel molecules. Rather than direct thermal evaporation from pores or the hydrogel network, water molecules evaporate from the liquid–vapor interface as hydrogen bonds between the cluster and water break. This process reduces the enthalpy of water within the hydrogel pores. Following evaporation, air replaces the pore, enabling further solar absorption and subsequent evaporation. However, for

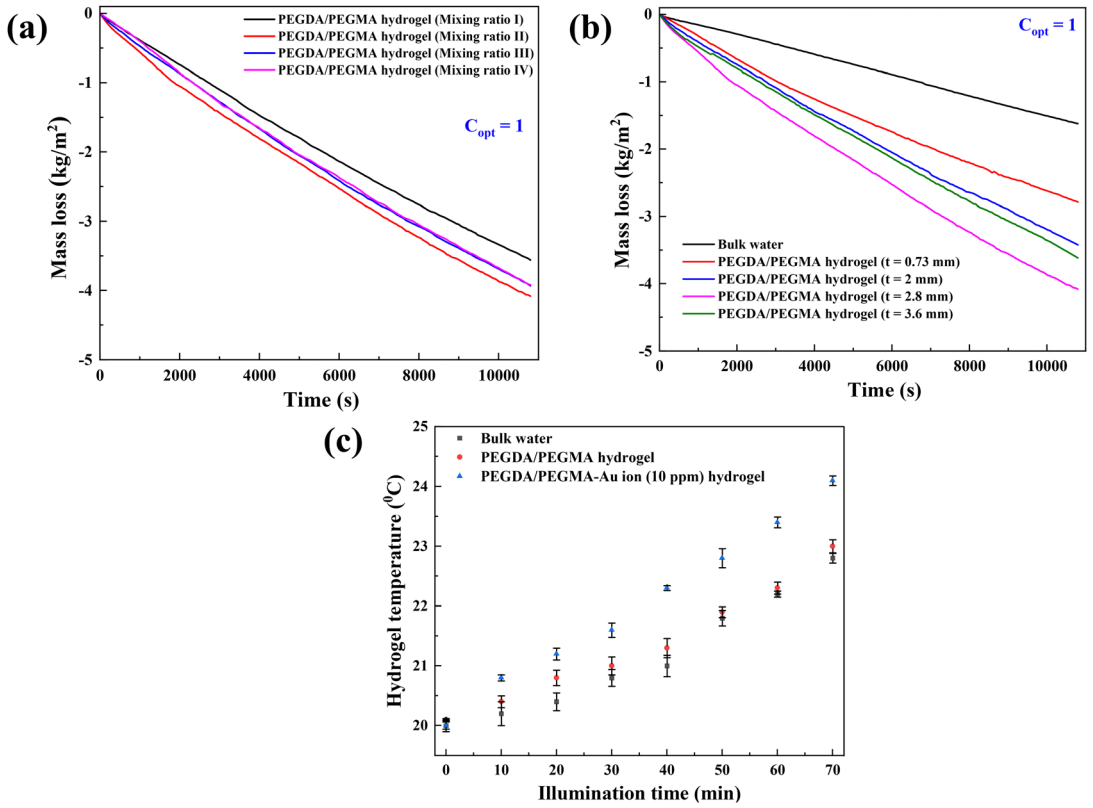

Fig. 2 Rate of mass loss of water in hydrogels of (a) varying mixing ratios, (b) varying thickness under 1-sun illumination, and (c) variation of interface temperature with respect to time under 1 sun illumination.

thickness exceeding 2.8 mm, the water transport path from bulk water to the hydrogel surface increases[29,30] while light absorption decreases beyond a certain thickness. Consequently, the optimum thickness is determined by balancing the length of the water transport path with the available water for evaporation within a hydrogel. In this study, an optimum thickness of 2.8 mm was identified as the best suited device, resulting in a maximum evaporation rate of 1.36 kg m^{-2} h^{-1}.

Evaporation enhancement using Au-ion in the hydrogel

Previous research has shown the effectiveness of enhancing solar absorption efficiency through the creation of composite polymer hydrogels that incorporate nanoparticles of Ag, Au, and Pt into hydrogel formulations.[42–45] However, the fabrication of Au nanoparticles (AuNPs) within a PEGDA/PEGMA hydrogel matrix remains unexplored. In this study, we present a novel approach for synthesizing a complex Au nanoparticle–hydrogel composite, diverging from the direct mixture of AuNPs with the hydrogel. This innovative method shows promise for various applications beyond SSG processes.[46,47] Various concentrations of gold precursor solutions (5, 10, 15 and 20 ppm of $HAuCl_4$, 10 mM) were added into the prepared hydrogel solution and cured under UV radiation (see the materials and methods section for details of the preparation). The incorporation of Au ion solution into the hydrogel under UV light converts the resultant solution into a hydrogel containing AuNPs (~100 nm) through the photoreduction of Au^{3+} ion within the PEGDA/PEGMA polymer networks.[48,49] Indeed, the formation of nanoparticles on the hydrogel surface is confirmed by the FE-SEM images obtained after the preparation of PEGDA/PEGMA-Au ion hydrogel. Fig. 3a represents the FE-SEM images of hydrogel only, while Fig. 3b and c illustrate the formation and agglomeration of AuNPs, further corroborated by the EDS spectra (inset image). Various-sized nanoparticles can also be produced by increasing the sonication time before curing the hydrogel solution. The size and content of Au NPs in the nanocomposite hydrogel can be controlled by adjusting the concentrations of the monomer and Au ions.[50] The comprehensive examination of nanoparticle formation is beyond the scope of the present study and will be addressed in future work. The highly porous structure and hydrophilic nature of the hydrogel facilitates high capillary actions and continuous water replenishment. To assess the potential alteration in surface wettability of hydrogels following nanoparticle incorporation, contact angles are measured, as depicted in Fig. 3d. The findings indicate an increased wettability of the hydrogels in the presence of nanoparticles.

Solar evaporation experiments are conducted under the same conditions as previously stated, utilizing PEGDA/PEGMA-Au-ion hydrogels of various concentrations (5, 10, 15 and 20 ppm), with the corresponding evaporation rates illustrated in Fig. 4a. Notably, the evaporation rate increases with the rising concentration of Au ions up to 10 ppm, but decreases thereafter. This evaporation mechanism is elucidated through the schematic diagram presented in Fig. 4b. When solar incident light illuminates the surface of the PEGDA/PEGMA-Au ion hydrogel, the hydrogel

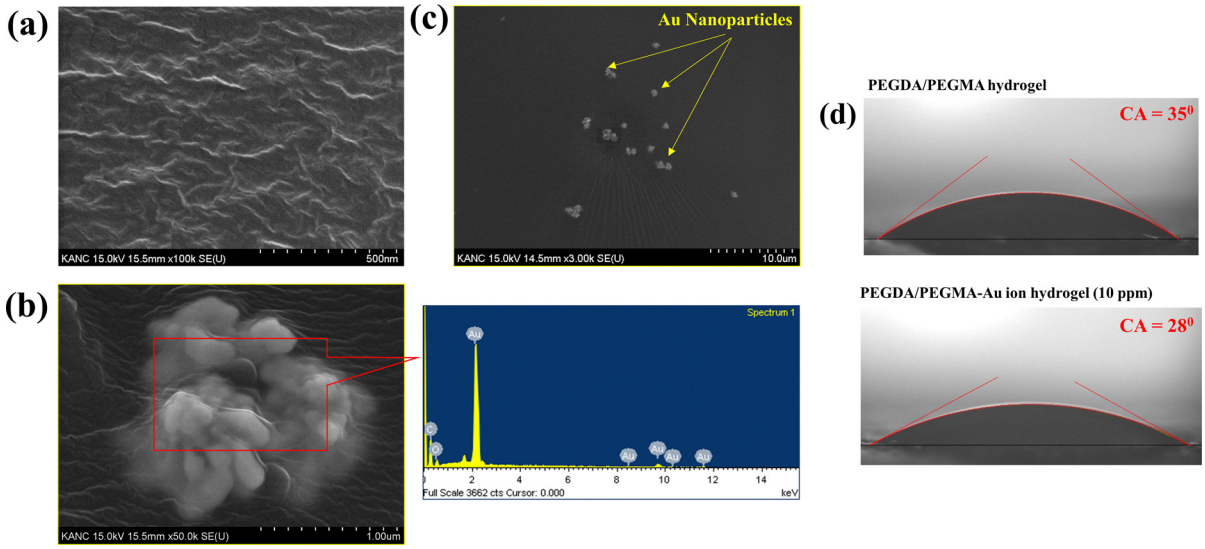

Fig. 3 FE-SEM images of (a) hydrogel only and (b) hydrogel + Au-ion (inset: the EDS result). (c) Formation of nanoparticle clusters in the hydrogel + Au-ion (20 ppm) and (d) contact angle measurement of water on the PEGDA/PEGMA and PEGDA/PEGMA-Au ion (10 ppm) hydrogels.

absorbs light due to its semi-transparency nature. Consequently, the light penetrates the entire thickness of the hydrogel, while the gold nanoparticles formed within the hydrogel absorb a portion of the light radiation (see the light absorption spectra, Fig. 4c and in the ESI†). This absorption enhances the local surface temperature of the nanoparticles due to the surface plasmon resonance (SPR) effect.[51,52] The continuous incidence of light further excites the photoelectrons generated by the SPR effect, subsequently increasing the surface temperature of the nanoparticles. As a result, the water in the vicinity of the nanoparticle surface vaporizes into steam, which eventually escapes through the hydrogel pores to the surface due to

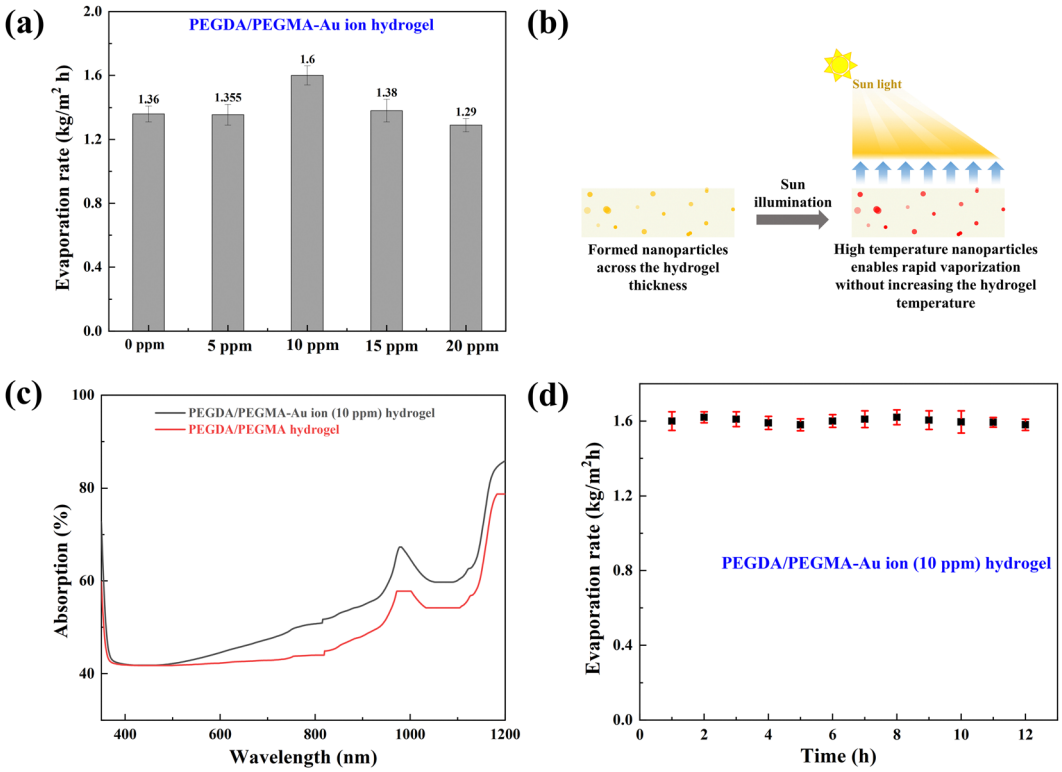

Fig. 4 (a) Evaporation rates of the PEGDA/PEGMA hydrogel at various Au ion concentrations. (b) Schematic diagram depicting evaporation mechanism. (c) Light absorption spectra of PEGDA/PEGMA and PEGDA/PEGMA-Au ion (10 ppm) hydrogels, and (d) stability of the PEGDA/PEGMA-Au ion (10 ppm) hydrogel over a 12 h period.

buoyancy. Importantly, heat transfer from the Au particles to the water is impeded within the hydrogel, as the steam is a poor thermal conductor. Thus, evaporation occurs without a significant increase in the overall temperature of the hydrogel,[53] as validated by the measured temperature during the evaporation process (Fig. 2c). Conversely, the decrease in evaporation rates with increasing Au ion concentration beyond 10 ppm could be attributed to the agglomeration of AuNPs within the hydrogel matrix at higher concentrations (Fig. 3c). This agglomeration results in the formation of larger nanoparticles within the hydrogel, potentially deforming the hydrogel structure and hindering water movement and, consequently, evaporation. Additionally, excessive deposition of nanoparticles within the hydrogel may impede the penetration of light and block the pores of the hydrogel, thereby hindering water uptake from the reservoir to the surface for evaporation. This phenomenon is corroborated by the observed decrease in the swelling ratio of PEGDA/PEGMA-Au ion (20 ppm) hydrogel as shown in Fig. S3 (ESI†).[54,55] Moreover, the stability of the present solar evaporation apparatus (PEGDA/PEGMA-Au ion, 10 ppm) has been examined, revealing consistent performance over a period of 12 hours as depicted in Fig. 4d.

Fig. 5a compares the rate of mass loss of bulk water, PEGDA/PEGMA and PEGDA/PEGMA-Au ion (10 ppm). The illumination results in a minor temperature increase of the bulk water and PEGDA/PEGMA-Au ion (10 ppm) of 3 °C and 4 °C, respectively[41] (Fig. 2c). The evaporation rate of PEGDA/PEGMA-Au ion at 10 ppm (1.6 kg m^{-2} h^{-1}) is approximately 1.2 times higher than that of the PEGDA/PEGMA hydrogel (1.36 kg m^{-2} h^{-1}) and 3 times higher than that of bulk water (0.53 kg m^{-2} h^{-1}). Similarly, Fig. 5b illustrates the rate of mass loss of PEGDA/PEGMA-Au ion (10 ppm) under various illumination conditions (no sun, 1 and 2-sun illumination). It is evident that the evaporation rate depends on solar intensity, with the maximum evaporation rate of 1.73 kg m^{-2} h^{-1} achieved under 2-sun illumination.

Solar efficiency

The solar efficiency (η) of the current solar device can be estimated using the following classical equation.[29]

$$\eta = \frac{\Delta m \times h_{lv}}{I} \quad (1)$$

where Δm is the net evaporation rate of the water during steady-state evaporation, h_{lv} is the total enthalpy of liquid–vapour phase change (sensible and latent heat of evaporation) and I is the solar illumination power density. The evaporation rate under dark conditions is subtracted from that under illumination conditions to obtain the actual evaporation rate for calculations. The calculated solar efficiency of the PEGDA/PEGMA and PEGDA/PEGMA-Au ion (10 ppm) hydrogels is found to be 60% and 77%, respectively. The increase in efficiency highlights the significance of AuNPs in the hydrogel, which enhances solar absorption by improving localized evaporation inside and on the surface of the hydrogel.

For the efficient operation of the current device, it is imperative to assess various heat losses from the hydrogel. The types of losses expected from the current device are depicted in Fig. 5c and a detailed calculation procedure is delineated in the ESI.† It is observed that radiation (~2.03%) and convective heat transfer loss (~2%) are relatively minor

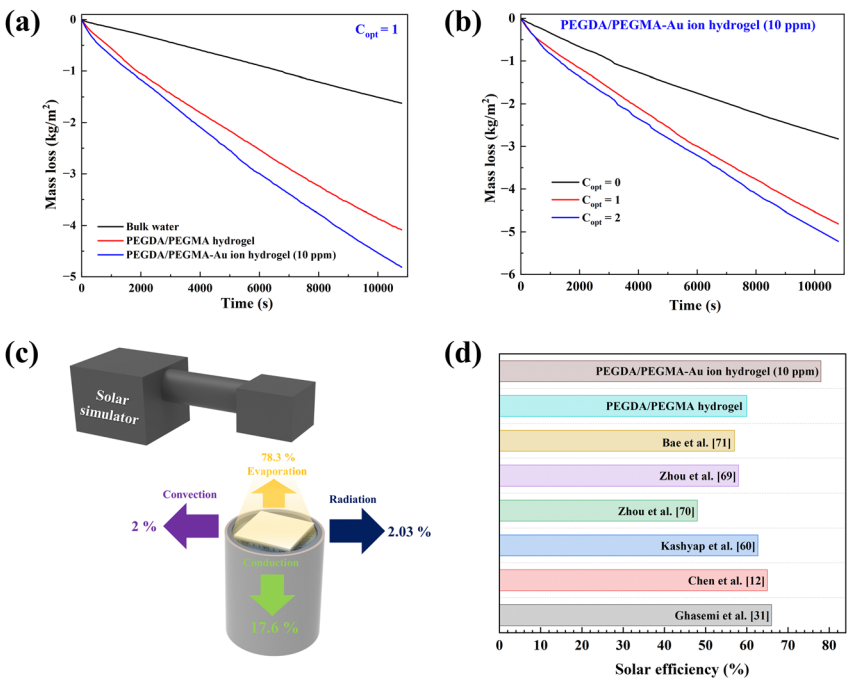

Fig. 5 Comparison of the rate of mass loss of (a) water, PEGDA/PEGMA, and PEGDA/PEGMA-Au ion (10 ppm) hydrogels under 1-sun illumination, (b) PEGDA/PEGMA-Au ion hydrogel (10 ppm) at various optical concentrations, (c) heat losses from the PEGDA/PEGMA-Au ion (10 ppm) solar evaporation setup under 1-sun illumination, and (d) comparison of the solar efficiencies with the literature.

compared to the predominant conduction loss (17.6%) from the hydrogel to the bulk water, which might be attributed to the utilization of a single-layer structure, differing from the multi-layered configurations employed by Ghasemi *et al.*,[31] Yuan *et al.*,[39] Liu *et al.*,[30] Yin *et al.*[29] and Xu *et al.*[21] Furthermore, the calculated evaporative heat loss (~78%) aligns closely with the measured solar evaporation efficiency (~77%). This high efficiency is attributed to the effective isolation of the bulk water from the external environment.[30,56,57] The evaporation rates of the current single-layer device are compared with those of devices incorporating multiple layers embedded with various materials, such as molybdenum sulfide,[58] flexible wood membranes,[12] 3D-printed cellulose/alginate/carbon black hydrogels[39] and $SMoS_2$-PH hydrogels[30] as summarized in Table 2. Notably, the maximum evaporation rate observed in the current case underscores the efficacy of the PEGDA/PEGMA-Au ion hydrogel, prepared *via* the crosslinking of two monomers, in providing a porous 3D network structure with abundant water channels. Additionally, the incorporation of AuNPs enhances light absorption, thereby activating the SPR effect to maximize evaporation. The enhanced evaporation rates observed surpass those in the current work, primarily due to the integration of light-absorbing materials such as MoS_2 and graphene, *etc.* in the design.

Additionally, the solar thermal efficiencies of the current device are compared with those of solar devices reported in the literature, as shown in Fig. 5d. The calculated solar efficiency for PEGDA/PEGMA-Au ion (10 ppm) is found to be larger than the values among all materials. This can be attributed to several desirable properties of the sample that contribute positively to the photo-thermal evaporation process.[69–71] Firstly, the hydrophilic and highly porous 3-D network structure facilitates continuous replenishment of water from the bulk to the upper hydrogel surface, thereby promoting efficient solar evaporation. Additionally, nanoparticles within the pores absorb solar illumination, exploiting the semi-transparent nature of the hydrogel, thereby enhancing evaporation rates without significantly raising the bulk water temperature. This approach minimizes heat loss and enhances the efficiency of the device.

For practical applications in solar steam generation, material performance and wettability play pivotal roles. Hydrogel materials, with their distinctive properties, have demonstrated considerable potential in interfacial evaporation applications. Moreover, the inherent flexibility of hydrogels enables them to conform to diverse surface shapes, thus expanding their suitability for a wide range of practical applications. In summary, the utilization of hydrogels in interfacial evaporation holds significant promise for advancing efficient and sustainable water treatment technologies.

Materials and methods

Materials used

Polyethylene glycol diacrylate (PEGDA, M_n = 250), polyethylene glycol methyl acrylate, (PEGMA, M_n = 480), phosphate-buffered saline (PBS) buffer solution and photo initiator (PI, 2-hydroxy-2-methylpropiophenone) were purchased from Sigma-Aldrich.

Table 2 Comparison of evaporation rates

Author	Hydrogel/material type	Evaporation rate (kg m^{-2} h^{-1})
Current work	Bulk water	0.53
	PEGDA/PEGMA hydrogel	1.36
		1.54[a]
	PEGDA/PEGMA-Au ion (10 ppm)	1.60
		1.73[a]
Chen *et al.*[12]	Flexible wood membrane (F-Wood/CNTs)	0.9
Sun *et al.*[18]	Copper sulfide-macroporous polyacrylamide (CuS-m-PAM)	1.5
Zhou *et al.*[20]	Reduced graphene oxide in PVA network hydrogel	2.5
Wu *et al.*[25]	Treated wood polydopamine (TW-2PDA)	1.38
Yin *et al.*[29]	Polyethylene glycol diacrylate (PEGDA) and polyaniline (p-PEGDA–PANi) + cellulose wrapped expanded polyethylene foam as a bottom layer	1.4
Liu *et al.*[30]	MoS_2-based porous hydrogel ($SMoS_2$-PH)	3.29
Ghasemi *et al.*[31]	Exfoliated graphite + carbon foam double layer structure (DLS)	1
Yuan *et al.*[39]	3D-printed cellulose/alginate/carbon black hydrogel (CACH)	1.33
Wang *et al.*[58]	Molybdenum sulfide (MoS_2)	1.27
Yang *et al.*[59]	Single-walled nanotube-MoS_2	1
Kashyap *et al.*[60]	Carbonized rayon (CR) along with exfoliated graphite + poly(3,4-ethylenedioxythiophene)–poly(styrenesulfonate) coating	1.01
Su *et al.*[61]	Graphene oxide (GO)	1.2
Xu *et al.*[62]	CuO nanowire mesh	1.42
Singh *et al.*[63]	Porous chitosan/carboxymethyl cellulose hydrogel with carbon dots	1.4
Ni *et al.*[64]	Blending of eco-friendly poly(vinyl alcohol), agarose, Fe^{3+} and tannic acid (TA)	1.89
Wang *et al.*[65]	Cellulose hydrogel (CH)/CNTs evaporators	2.56
Xu *et al.*[66]	Chitosan/PAAm/PPy hydrogel	2.3
Fu *et al.*[67]	Graphene aerogel (GA)	2.6
Wang *et al.*[68]	Wood-PVA-CNT device	1.37

[a] Evaporation rate under 2-sun illumination.

Gold(III) chloride trihydrate ($HAuCl_4 \cdot 3H_2O$, 48.5–50.25%) was also obtained from Sigma-Aldrich. The copper mesh (#50, 0.23 mm wire diameter) was purchased from Alfa Aesar. Throughout the experiments, deionized (DI) water was used.

Fabrication of experimental setup

For the evaporation experiment, a mesh was integrated with the hydrogel to enhance the mechanical strength (Fig. 1a). A hydrophobic copper mesh #50 (as received) was cut into 10 mm × 10 mm and attached to a laser cut acrylic sheet (Fig. S1a(i), ESI†) of the same dimensions (Fig. S1a(ii), ESI†). The prepared setup was then attached to the PDMS molds of varying thickness (Fig. S1a(iii), ESI†), and the prepared hydrogel was poured and cured under UV light. Subsequently, the hydrogel-embedded mesh was fitted onto a container filled with DI water (Fig. S1a(iv), ESI†). The seam between the acrylic sheet and the side wall of the bulk water container was meticulously sealed with parafilm to ensure that the evaporation occurred solely from the hydrogel surface. Then, the liquid PEGDA hydrogel or hydrogel containing Au ion solution was poured into the mold to prepare PEGDA/PEGMA hydrogel and PEGDA/PEGMA-Au ion hydrogel, respectively, for the evaporation experiments (Fig. S1a(v), ESI†).

Preparation of gold ion solution and hydrogel solution. Ionic gold solutions ($HAuCl_4$, 10 mM) were prepared by dissolving the compound in deionized (DI) water. For the evaporation experiments in this study, four different combinations of hydrogel were prepared by considering various mixing ratios of PEGDA, PEGMA, PI and PBS, as detailed in Table 1. Initially, for each mixing ratio (10 mL solution), 1500 μL of PEGDA and 1500 μL of PEGMA were added to a container and mixed using a vortex mixer. Subsequently, 600 μL of PI was introduced into the solution, followed by the addition of 7000 μL of PBS. The resulting solution was then subjected to sonication for approximately 1 h. Next, the hydrogel solution was poured into molds of various thickness (0.73, 2, 2.8 and 3.6 mm) and irradiated with ultraviolet (UV) light at an energy of 1200 mJ cm^{-2} from both sides for appropriate curing, resulting in the formation of the PEGDA/PEGMA hydrogel. For the preparation of the PEGDA/PEGMA-Au ion hydrogel, four different concentrations (5, 10, 15 and 20 ppm) of gold ionic solution were added to the hydrogel and sonicated for approximately 30 minutes. Then, the hydrogel solution was poured into molds with a thickness of 2.8 mm for polymerization under UV light (1200 mJ cm^{-2}).

Characterizations. The light absorption spectra were obtained using a UV-vis-NIR spectrophotometer (Agilent Technologies, Cary 5000). An integrating sphere was used to collect the reflected light. Gold nanoparticle formation was verified using a field emission scanning electron microscope (FE-SEM, Hitachi-SU8600, KANC, South Korea) and further confirmed by electron dispersive spectroscopy (EDS, Hitachi-SU8600, KANC, South Korea). Hydrogel solutions were cured using an ultraviolet mask aligner (MDA-4001LJ). Temperature measurements were taken using an infrared (IR) camera (FLIR, ResearchIR Max-SC655). Solar evaporation tests were conducted under simulated 1 and 2 sun illuminations using a portable solar simulator (PEC-L01). Water contact angles on hydrogel samples were measured with a contact angle analyser (Smartdrop, FEMTOFAB SDS-TEZD-10013, Korea), and the results were averaged over three measurements.

Measurement of swelling ratio. Swelling ratios (SR) are measured using the volume method based on eqn (2):

$$\mathrm{SR}\left(\mathrm{g\,g^{-1}}\right) = \frac{W_s - W_d}{W_d} \quad (2)$$

where W_d is the weight of the dry hydrogel and W_s is the weight of the fully swollen hydrogel.

Conclusions

The present study introduces a facile, robust, and highly efficient solar evaporation setup featuring a 3D network of hydrophilic pores within a single-layer semi-transparent hydrogel structure, tailored for optimal evaporation performance. Our device consistently achieves a maximum evaporation rate of 1.6 kg m^{-2} h^{-1}, maintaining stability over a 12-hour period and delivering a high efficiency of 77% using a PEGDA/PEGMA-Au ion hydrogel under 1-sun illumination and room temperature conditions, comparable to those of other materials with a double or multi-layered structure reported in the literature. The consistency between the calculated evaporative heat loss from the device and the evaporation efficiency attests to the superior performance of our device. The highly porous structure, efficient solar absorption facilitated by nanoparticle incorporation, and the exceptional swelling ratio collectively contribute to maximize the efficiency. Notably, the abundant pores in the hydrogel structure enable a continuous flow of water from the bulk to the surface. The semi-transparent nature of the hydrogel facilitates the penetration of solar illumination, while efficient evaporation occurs through the photomolecular effect without significantly increasing the hydrogel temperature. Enhanced light absorption, driven by the surface plasmon resonance of the nanoparticles, further accelerates evaporation rates.

Author contributions

A. R. P.: conducted experiments, conceptualization, writing – original draft, methodology, and formal analysis. Y. S. K., C. B., Y. J. H., I. C. and C. L.: writing – review & editing. C. L.: supervision, writing – review & editing, project administration, and data curation.

Conflicts of interest

There are no conflicts to declare.

Acknowledgements

This research was supported by the Basic Research Program (2023R1A2C2006961, 2023R1A2C2003947) and the Basic Research Laboratory (2021R1A4A3027074) through the National Research

Foundation of Korea (NRF) funded by the Ministry of Science and ICT, Korea.

References

1 I. Haddeland, J. Heinke, H. Biemans, S. Eisner, M. Flörke, N. Hanasaki, M. Konzmann, F. Ludwig, Y. Masaki, J. Schewe, T. Stacke, Z. D. Tessler, Y. Wada and D. Wisser, *Proc. Natl. Acad. Sci. U. S. A.*, 2014, **111**, 3251–3256.
2 M. M. Mekonnen and A. Y. Hoekstra, *Sci. Adv.*, 2016, **2**(2), e1500323.
3 V. D. Dao, N. H. Vu and S. Yun, *Nano Energy*, 2020, **68**, 104324.
4 S. A. Kalogirou, *Prog. Energy Combust. Sci.*, 2004, **30**, 231–295.
5 S. Kalogirou, *Energy*, 1997, **22**, 69–81.
6 D. Zhao, H. Duan, S. Yu, Y. Zhang, J. He, X. Quan, P. Tao, W. Shang, J. Wu, C. Song and T. Deng, *Sci. Rep.*, 2015, **5**, 17276.
7 S. W. Sharshir, A. M. Algazzar, K. A. Elmaadawy, A. W. Kandeal, M. R. Elkadeem, T. Arunkumar, J. Zang and N. Yang, *Desalination*, 2020, **491**, 114564.
8 H. Ren, M. Tang, B. Guan, K. Wang, J. Yang, F. Wang, M. Wang, J. Shan, Z. Chen, D. Wei, H. Peng and Z. Liu, *Adv. Mater.*, 2017, **29**(38), 1702590.
9 L. Ruiz-Pérez, L. Rizzello, J. Wang, N. Li, G. Battaglia and Y. Pei, *Soft Matter*, 2020, **16**, 4569–4573.
10 C. Liu, J. Huang, C. Hsiung, Y. Tian, J. Wang, Y. Han and A. Fratalocchi, *Adv. Sustainable Syst.*, 2017, **1**, 1600013.
11 L. Zhang, B. Tang, J. Wu, R. Li and P. Wang, *Adv. Mater.*, 2015, **27**, 4889–4894.
12 C. Chen, Y. Li, J. Song, Z. Yang, Y. Kuang, E. Hitz, C. Jia, A. Gong, F. Jiang, J. Y. Zhu, B. Yang, J. Xie and L. Hu, *Adv. Mater.*, 2017, **29**, 1701756.
13 Y. Zeng, J. Yao, B. A. Horri, K. Wang, Y. Wu, D. Li and H. Wang, *Energy Environ. Sci.*, 2011, **4**, 4074.
14 G. Baffou and R. Quidant, *Laser Photonics Rev.*, 2013, **7**, 171–187.
15 E. Ju, Z. Li, M. Li, K. Dong, J. Ren and X. Qu, *Chem. Commun.*, 2013, **49**, 9048–9050.
16 L. Li, K. Liang, Z. Hua, M. Zou, K. Chen and W. Wang, *Polym. Chem.*, 2015, **6**, 2290–2296.
17 H. Sun, X. Li, J. Chen, H. Zhu, H. Miao, Y. Li, X. Liu and G. Shi, *Soft Matter*, 2021, **17**, 4730–4737.
18 Y. Sun, J. Gao, Y. Liu, H. Kang, M. Xie, F. Wu and H. Qiu, *Chem. Eng. Sci.*, 2019, **207**, 516–526.
19 M. Zhu, X. Liu, Y. Tian, A. Caratenuto, F. Chen and Y. Zheng, *Sci. Rep.*, 2022, **22**, 4403.
20 X. Zhou, F. Zhao, Y. Guo, Y. Zhang and G. Yu, *Energy Environ. Sci.*, 2018, **11**, 1985–1992.
21 Y. Xu, B. Lv, Y. Yang, X. Fan, Y. Yu, C. Song and Y. Liu, *Desalination*, 2021, **517**, 115260.
22 K. Sheng, M. Tian, J. Wang, J. Zhu and Y. Zhang, *Desalination*, 2022, **541**, 116060.
23 Z. Sun, J. Wang, Q. Wu, Z. Wang, Z. Wang, J. Sun and C. J. Liu, *Adv. Funct. Mater.*, 2019, **29**, 1901312.
24 Y. Guo, X. Zhou, F. Zhao, J. Bae, B. Rosenberger and G. Yu, *ACS Nano*, 2019, **13**, 7913–7919.
25 X. Wu, G. Y. Chen, W. Zhang, X. Liu and H. Xu, *Adv. Sustainable Syst.*, 2017, **1**, 1700046.
26 Q. Chen, Z. Pei, Y. Xu, Z. Li, Y. Yang, Y. Wei and Y. Ji, *Chem. Sci.*, 2018, **9**, 623–628.
27 X. Lin, J. Chen, Z. Yuan, M. Yang, G. Chen, D. Yu, M. Zhang, W. Hong and X. Chen, *J. Mater. Chem. A*, 2018, **6**, 4642–4648.
28 V. Gopishetty, I. Tokarev and S. Minko, *J. Mater. Chem.*, 2012, **22**, 19482.
29 X. Yin, Y. Zhang, Q. Guo, X. Cai, J. Xiao, Z. Ding and J. Yang, *ACS Appl. Mater. Interfaces*, 2018, **10**, 10998–11007.
30 P. Liu, Y. B. Hu, X. Y. Li, L. Xu, C. Chen, B. Yuan and M. L. Fu, *Angew. Chem., Int. Ed.*, 2022, **61**, e202208587.
31 H. Ghasemi, G. Ni, A. M. Marconnet, J. Loomis, S. Yerci, N. Miljkovic and G. Chen, *Nat. Commun.*, 2014, **5**, 4449.
32 K. L. Spiller, S. J. Laurencin and A. M. Lowman, *J. Biomed. Mater. Res., Part B*, 2009, **90B**, 752–759.
33 I. I. Preobrazhenskiy and V. I. Putlyaev, *Mendeleev Commun.*, 2023, **33**, 83–85.
34 H. Zhang, L. Wang, L. Song, G. Niu, H. Cao, G. Wang, H. Yang and S. Zhu, *J. Appl. Polym. Sci.*, 2011, **121**, 531–540.
35 K. O'Donnell, A. Boyd and B. J. Meenan, *Materials*, 2019, **12**(20), 3381.
36 Y. Zu, Y. Zhang, X. Zhao, C. Shan, S. Zu, K. Wang, Y. Li and Y. Ge, *Int. J. Biol. Macromol.*, 2012, **50**, 82–87.
37 N. G. Bel'nikevich, N. V. Bobrova, V. Y. Elokhovskii, Z. F. Zoolshoev, M. A. Smirnov and G. K. Elyashevich, *Russ. J. Appl. Chem.*, 2011, **84**, 2106–2113.
38 J. A. Beamish, J. Zhu, K. Kottke-Marchant and R. E. Marchant, *J. Biomed. Mater. Res., Part A*, 2010, **92A**, 441–450.
39 J. Yuan, X. Lei, C. Yi, H. Jiang, F. Liu and G. J. Cheng, *Chem. Eng.*, 2022, **430**(2), 132765.
40 M. Miyazaki, A. Fujii, T. Ebata and N. Mikami, *Science*, 2004, **304**(5674), 1134–1137.
41 Y. Tu, J. Zhou, S. Lin, M. Alshrah, X. Zhao and G. Chen, *Proc. Natl. Acad. Sci. U. S. A.*, 2023, **120**(45), e2312751120.
42 C. Hou, K. Ma, T. Jiao, R. Xing, K. Li, J. Zhou and L. Zhang, *RSC Adv.*, 2016, **6**, 110799–110807.
43 B. Miranda, R. Moretta, S. De Martino, P. Dardano, I. Rea, C. Forestiere and L. De Stefano, *J. Appl. Phys.*, 2021, **129**, 033101.
44 C. Díaz-Cruz, G. Alonso Nuñez, H. Espinoza-Gómez and L. Z. Flores-López, *Eur. Polym. J.*, 2016, **83**, 265–277.
45 Y. A. R. Nuñez, R. I. Castro, F. A. Arenas, Z. E. López-Cabaña, G. Carreño, V. Carrasco-Sánchez, A. Marican, J. Villaseñor, E. Vargas, L. S. Santos and E. F. Durán-Lara, *Polymers*, 2019, **11**(4), 716.
46 X. Dong, J. Liang, A. Yang, Z. Qian, D. Kong and F. Lv, *Biomaterials*, 2019, **209**, 111–125.
47 Z. Wang, Q. Ye, S. Yu and B. Akhavan, *Adv. Healthcare Mater.*, 2023, **12**, 2300105.
48 Z. Batool, G. Muhammad, M. M. Iqbal, M. S. Aslam, M. A. Raza, N. Sajjad, M. Abdullah, N. Akhtar, A. Syed, A. M. Elgorban, S. S. Al-Rejaie and Z. Shafiq, *Sci. Rep.*, 2022, **12**, 6575.

49 C. Luo, Y. Zhang, X. Zeng, Y. Zeng and Y. Wang, *J. Colloid Interface Sci.*, 2005, **288**, 444–448.
50 C. H. Zhu, Z. Bin Hai, C. H. Cui, H. H. Li, J. F. Chen and S. H. Yu, *Small*, 2012, **8**, 930–936.
51 J. R. Adleman, D. A. Boyd, D. G. Goodwin and D. Psaltis, *Nano Lett.*, 2009, **9**, 4417–4423.
52 O. Neumann, A. S. Urban, J. Day, S. Lal, P. Nordlander and N. J. Halas, *ACS Nano*, 2013, **7**, 42–49.
53 A. Polman, *ACS Nano*, 2013, **7**, 15–18.
54 Y. M. Mohan, T. Premkumar, K. Lee and K. E. Geckeler, *Macromol. Rapid Commun.*, 2006, **27**, 1346–1354.
55 L. Daniel-da-Silva, A. M. Salgueiro and T. Trindade, *Gold Bull.*, 2013, **46**, 25–33.
56 L. Zhao, P. Wang, J. Tian, J. Wang, L. Li, L. Xu, Y. Wang, X. Fei and Y. Li, *Sci. Total Environ.*, 2019, **668**, 153–160.
57 X. Li, C. Yang, Z. Chen, S. Liu, J. Li and S. Li, *ACS ES&T Water*, 2023, **3**(7), 1740–1746.
58 Q. Wang, Q. Guo, F. Jia, Y. Li and S. Song, *ACS Appl. Mater. Interfaces*, 2020, **12**, 32673–32680.
59 X. Yang, Y. Yang, L. Fu, M. Zou, Z. Li, A. Cao and Q. Yuan, *Adv. Funct. Mater.*, 2018, **28**, 1704505.
60 V. Kashyap, A. Al-Bayati, S. M. Sajadi, P. Irajizad, S. H. Wang and H. Ghasemi, *J. Mater. Chem. A*, 2017, **5**, 15227–15234.
61 H. Su, J. Zhou, L. Miao, J. Shi, Y. Gu, P. Wang, Y. Tian, X. Mu, A. Wei, L. Huang, S. Chen and Z. Deng, *Sustainable Mater. Technol.*, 2019, **20**, e00095.
62 Y. Xu, J. Ma, Y. Han, J. Zhang, F. Cui, Y. Zhao, X. Li and W. Wang, *ACS Sustainable Chem. Eng.*, 2019, **7**, 5476–5485.
63 S. Singh, N. Shauloff and R. Jelinek, *ACS Sustainable Chem. Eng.*, 2019, **7**, 13186–13194.
64 A. Ni, D. Fu, P. Lin, X. Wang, Y. Xia, X. Han and T. Zhang, *J. Colloid Interface Sci.*, 2023, **647**, 344–353.
65 Z. Wang, R. Jin, S. Zhang, X. Han, P. Guo, L. Jiang and L. Heng, *Adv. Funct. Mater.*, 2023, **33**, 2306806.
66 T. Xu, Y. Xu, J. Wang, H. Lu, W. Liu and J. Wang, *Chem. Eng.*, 2021, **415**, 128893.
67 Y. Fu, G. Wang, T. Mei, J. Li, J. Wang and X. Wang, *ACS Sustainable Chem. Eng.*, 2017, **5**, 4665–4671.
68 Z. Wang, P. Guo, L. Heng and L. Jiang, *Matter*, 2021, **4**, 1274–1286.
69 L. Zhou, S. Zhuang, C. He, Y. Tan, Z. Wang and J. Zhu, *Nano Energy*, 2017, **32**, 195–200.
70 L. Zhou, Y. Tan, J. Wang, W. Xu, Y. Yuan, W. Cai, S. Zhu and J. Zhu, *Nat. Photonics*, 2016, **10**, 393–398.
71 K. Bae, G. Kang, S. K. Cho, W. Park, K. Kim and W. J. Padilla, *Nat. Commun.*, 2015, **6**, 10103.